






Unified wall-resolved and wall-modeled method for large-eddy simulations of compressible wall-bounded flows

Francesco De Vanna ^{1,*} Michele Cogo ¹ Matteo Bernardini ²
Francesco Picano ³ and Ernesto Benini ¹

¹*Department of Industrial Engineering, Università degli Studi di Padova, Via Venezia 1, 35131 Padova, Italy*

²*Department of Mechanical and Aeronautical Engineering, Università di Roma "La Sapienza," Rome, Italy*

³*Department of Industrial Engineering and CISAS, Università degli Studi di Padova, Via Venezia 1, 35131 Padova, Italy*



(Received 5 November 2020; accepted 8 March 2021; published 29 March 2021)

We present a general strategy to unify wall-resolved and wall-modeled large-eddy simulation (LES) approaches for turbulent wall-bounded compressible flows. The proposed technique allows one to impose the proper wall stress and heat flux, preserving the no-slip and the isothermal and adiabatic conditions for the velocity and temperature fields, respectively. The approach results in a minimal intrusive algorithm that automatically switches between wall-resolved and wall-modeled LES according to the local near-wall resolution. The methodology is discussed and implemented in a flow solver based on high-order finite difference schemes, the application of which in the context of wall-modeled LES has been less explored in the available literature. Numerical simulations of canonical turbulent channel flow and spatially evolving boundary layer are performed in a wide range of Mach and Reynolds numbers. The results highlight the ability of the present method to accurately reproduce the outer layer turbulent dynamics, with a minimal influence of the near-wall grid resolution. In particular, velocity statistics and two-point spatial correlations are in good agreement with reference direct numerical simulation and wall-resolved LES, confirming the potential of the proposed approach for predictive analysis of wall-bounded flows at high-Reynolds number.

DOI: [10.1103/PhysRevFluids.6.034614](https://doi.org/10.1103/PhysRevFluids.6.034614)

I. INTRODUCTION

Wall turbulence plays a fundamental role in a broad range of physical phenomena and engineering applications. Future technological improvements concerning external aerodynamics, turbomachinery, propulsive, and hydrodynamics systems require a deeper comprehension of fluid mechanics over solid walls [1–5]. Most of these applications involve turbulent flows, that are inherently characterized by small-scale eddies in the inner layer playing a fundamental role in determining friction drag and heat transfer at the wall. They represent a critical issue for any predictive numerical model.

One major problem in simulating wall turbulence is that close to the wall the energy-carrying structures scale with the viscous length, $\delta_v = \nu/u_\tau$, instead of the local boundary layer thickness, δ . Here $u_\tau = \sqrt{\tau_w/\rho_w}$ denotes the friction velocity and ν denotes the kinematic viscosity of the flow. Therefore, as the friction Reynolds number ($\text{Re}_\tau = \delta/\delta_v$) increases, the near-wall eddies decrease in size relative to the boundary layer (BL) thickness. Although direct numerical simulation (DNS) and large-eddy simulation (LES) can accurately predict the physics of turbulent wall-bounded flows,

*Corresponding author: francesco.devanna@unipd.it

these strategies become prohibitively expensive at high-Reynolds conditions. As a consequence, Reynolds averaged Navier-Stokes (RANS) approaches are largely preferred in the engineering practice, even if the errors introduced by modeling all turbulent scales reduce the predictive capability, particularly for flows with large and massive separations. In this regard, Chapman [6] and Choi and Moin [7] estimated that the number of grid points necessary to resolve the near-wall eddies for DNS and wall-resolved LES (WRLES) is about $N_{\text{DNS}} \sim \text{Re}_L^{37/14}$ and $N_{\text{WR}} \sim \text{Re}_L^{13/7}$ respectively, where Re_L is the Reynolds number based on a characteristic length. Despite the more favorable computational cost of WRLES compared to DNS, the nearly quadratic relation with the Reynolds number is still too demanding. Choi and Moin [7] also provided an asymptotic relation for wall-modeled LES (WMLES), i.e., a LES methodology where the near-wall region is modeled, estimating that N_{WM} is approximately a linear function of Re_L . This makes WMLES an attractive choice to simulate a strongly time-dependent wall-bounded flow in a reasonable amount of time and with affordable computational resources.

The theoretical investigation of the near-wall region goes back to the beginning of the 20th century. The first *law of the wall*, proposed by von Kármán [8], is a very popular analytical distribution that can be considered a milestone of near-wall turbulence theory. Over the years, several extensions of this law have been proposed [9–11] to account for the discrepancies found among flows in different geometries and to extend the original description to the low-Reynolds regime. The universal character of these near-wall analytical descriptions has led to a great interest in the development of *wall functions*, an idea originally introduced by Launder and Spalding [12] and then pursued by many others (see, e.g., Craft *et al.* [13]). Wall functions prevent the need to resolve the near-wall region and can be employed to design off-wall boundary conditions [14,15].

In the context of WMLES, available methods generally fall into two different categories: (i) hybrid LES-RANS approaches and (ii) wall-stress model approaches [16,17]. While in the former the computational domain is divided into near-wall and outer regions where RANS and LES are, respectively, employed, the latter technique imposes a wall stress computed on an independent grid that provides the proper boundary conditions to the LES field, covering the whole domain. This distinction implies that hybrid LES-RANS techniques focus on blending the RANS-type turbulent eddy viscosity near the wall with an LES-type subgrid scale (SGS) eddy viscosity away from the boundaries, using a single mesh (see, e.g., Menter [18]). Conversely, the WMLES approach aims at feeding the information of the wall shear stress and heat flux computed with an external model, either algebraic or differential, into the LES field. In this regard, numerous contributions have appeared in the last decades. Cabot and Moin [19] reviewed low-order wall-modeling approaches combined with the dynamic Smagorinsky SGS model. The authors examined both attached and separated flows and discussed a novel method to develop wall models from optimal control theory. Wang and Moin [20] proposed a dynamically adjusted wall-modeled eddy viscosity method for LES of turbulent boundary layer flows past an asymmetric trailing edge. The study showed that low-order velocity statistics were in good agreement with corresponding WRLES at a small fraction of the original computational cost. Temmerman *et al.* [21] performed a systematic investigation on the LES of periodic channels with hill-shaped obstructions to assess the predictive accuracy concerning resolution and modeling issues. Kawai and Asada [22] extended the work of Wang and Moin [20] by considering a nonequilibrium wall model based on unsteady three-dimensional RANS equations. The method accounts for a new dynamic eddy viscosity and conductivity model that corrects the effect of the resolved Reynolds stress and heat flux on the skin friction and the near-wall thermodynamics. Bose and Moin [23] proposed a dynamic procedure to establish a local slip length for the wall model to remove any *a priori* specified coefficient. Park and Moin [24] investigated the capability of WMLES in predicting the transitional and separated regions of the flow over an airfoil near stall condition at a high Reynolds number. The comparisons between equilibrium and nonequilibrium wall models highlight the importance of including the nonequilibrium effects. More recent developments about WMLES are documented in Larsson *et al.* [17], Bose and Park [25], and Yang and Lv [26] where applications of WMLES to complex flows and high-speed conditions are reported.

Despite the importance and wide interest for this subject, WRLES and WMLES techniques are still separate strategies in the field of wall-turbulence applications, and no significant attempts have been documented to blend them in order to exploit the full potential of the two methods. Consider for instance the simulation of the flow over a wing at a high Reynolds number. WMLES represents a useful tool to predict the flow dynamics at a reasonable computational cost. However, since the near-wall regions can be very different depending on the position considered (laminar, transitional, turbulent), local grid requirements can vary significantly. Moreover, while high-Reynolds-number turbulent zones have to be simulated relying on a wall model, regions characterized by incipient separation, in which the velocity gradient is locally zero, might be directly computed on the computational grid. Unfortunately, the use of pure WMLES prevents the possibility to resolve these portions of the flow. Therefore, a unified strategy that can merge the advantages of WMLES and WRLES keeping the overall computational cost affordable is highly desirable.

The present paper aims at enabling a smooth transition between WRLES and WMLES, designing a robust algorithm that dynamically adapts the wall treatment. In particular, we propose a unified method that employs augmented turbulent viscosity and diffusivity at the wall location and allows one to preserve the no-slip and the isothermal and adiabatic conditions. Such an approach was partially explored in the field of incompressible flows (see, e.g., Krajnović and Davidson [27] and Mukha *et al.* [28]) but it has never been addressed in compressible conditions. Moreover, we discuss the implementation of the method in the context of high-order, energy-preserving finite difference (FD) schemes, which represent the ideal solution for LES, allowing for fine control of the numerical dissipation.

The paper is organized as follows: in Sec. II, the governing equations and the mathematical models are presented and discussed. In Sec. III, the numerical method is described focusing on the discrete treatment of the filtered Navier-Stokes equations and the coupling with the wall model. Simulation results are discussed in Sec. IV, where detailed comparisons of the present method with reference DNS and LES are provided. Finally, Sec. V summarizes the conclusions.

II. GOVERNING EQUATIONS AND NUMERICAL MODEL

This study has been conducted using URANOS (Unsteady Robust All-Around Navier Stokes Solver) [29–31], a DNS and LES solver developed at the University of Padova. The code solves the filtered compressible Navier-Stokes equations in a conservative formulation. Using the Reynolds ($\phi = \bar{\phi} + \phi'$) and the Favre ($\phi = \bar{\phi} + \phi''$, $\bar{\phi} = \overline{\rho\phi}/\bar{\rho}$) decompositions, where the overbar denotes the averaging process in the homogenous space directions and in time, the model reads as follows:

$$\frac{\partial \bar{\rho}}{\partial t} = -\frac{\partial \bar{\rho} \tilde{u}_j}{\partial x_j}, \quad (1a)$$

$$\frac{\partial \bar{\rho} \tilde{u}_i}{\partial t} + \frac{\partial \bar{\rho} \tilde{u}_i \tilde{u}_j}{\partial x_j} = -\frac{\partial \bar{p}_i \delta_{ij}}{\partial x_j} + \frac{\partial \bar{\tau}_{ij}}{\partial x_j} - \frac{\partial T_{ij}^{\text{SGS}}}{\partial x_j}, \quad (1b)$$

$$\frac{\partial \bar{\rho} \tilde{E}}{\partial t} + \frac{\partial \bar{\rho} \tilde{u}_j \tilde{E}}{\partial x_j} = -\frac{\partial \bar{p} \tilde{u}_j}{\partial x_j} + \frac{\partial \tilde{u}_j \bar{\tau}_{ij}}{\partial x_j} - \frac{\partial \tilde{J}_j}{\partial x_j} - \frac{\partial E_j^{\text{SGS}}}{\partial x_j}. \quad (1c)$$

Here $\bar{\rho}$ is the filtered density, \tilde{u}_i denotes the Favre-averaged velocity component in the i th direction, \bar{p} is the filtered thermodynamic pressure, $\tilde{E} = \tilde{e} + \tilde{u}_i \tilde{u}_i / 2$ is the Favre-averaged total energy per unit mass, \tilde{J}_j is the j th component of the filtered molecular heat flux, and \tilde{e} is the Favre internal energy per unit mass. The thermodynamic variables are related by the ideal gas law, $\bar{p} = \bar{\rho} R \tilde{T}$, where \tilde{T} denotes the Favre temperature and R is the gas constant. The viscous stress tensor $\bar{\tau}_{ij}$ is expressed as

$$\bar{\tau}_{ij} = 2\mu(\tilde{T})(\tilde{S}_{ij} - \frac{1}{3}\tilde{S}_{kk}\delta_{ij}) \quad (2)$$

where $\mu(\tilde{T})$ is the molecular viscosity, that is assumed to obey Sutherland's law:

$$\mu(\tilde{T}) = \tilde{T}^{3/2} \left(\frac{T_0 + S}{\tilde{T} + S} \right) \quad (3)$$

where $T_0 = 273.15K$ and $S = 110.4K$ are empirical parameters. \tilde{S}_{ij} denotes the resolved strain-rate tensor, $\tilde{S}_{ij} = 1/2(\tilde{g}_{ij} + \tilde{g}_{ji})$, with $\tilde{g}_{ij} = \partial \tilde{u}_i / \partial x_j$ the resolved velocity gradient. The j th component of the filtered molecular heat flux is approximated using Fourier's law:

$$\tilde{J}_j = -\lambda(\tilde{T}) \frac{\partial \tilde{T}}{\partial x_j} \quad (4)$$

where $\lambda = \gamma R / (\gamma - 1) \mu(\tilde{T}) / \text{Pr}$ is the thermal conductivity. Here Pr denotes the molecular Prandtl number and $\gamma = c_p / c_v$ is the specific heat ratio, the values of which are set equal to 0.71 and 1.4, respectively.

The SGS stress tensor $T_{ij}^{\text{SGS}} = \overline{\rho u_i u_j} - \bar{\rho} \tilde{u}_i \tilde{u}_j$ is modeled as

$$T_{ij}^{\text{SGS}} - \frac{1}{3} T_{kk}^{\text{SGS}} \delta_{ij} = -2 \mu_{\text{SGS}} (\tilde{S}_{ij} - \frac{1}{3} \tilde{S}_{kk} \delta_{ij}) \quad (5)$$

where μ_{SGS} denotes the SGS viscosity and T_{kk}^{SGS} is the isotropic contribution. According to Garnier *et al.* [32], the latter assumes large values near shocks and discontinuities where (usually) the numerical schemes introduce a considerable amount of numerical dissipation to keep the solution stable. Therefore, this term is often overwhelmed by the numerical upwinding process, making its contribution negligible. In the present paper, the SGS viscosity is computed using the wall-adaptive large-eddy model by Nicoud and Ducros [33], according to which μ_{SGS} is expressed as

$$\mu_{\text{SGS}} = \bar{\rho} (C_w \Delta)^2 \frac{(S_{ij}^d S_{ij}^d)^{3/2}}{(S_{ij} S_{ij})^{5/2} + (S_{ij}^d S_{ij}^d)^{5/4}} \quad (6)$$

where

$$S_{ij}^d = \frac{1}{2} (\tilde{g}_{il} \tilde{g}_{lj} + \tilde{g}_{jl} \tilde{g}_{li}) - \frac{1}{3} \tilde{g}_{ml} \tilde{g}_{lm} \delta_{ij} \quad (7)$$

is the traceless symmetric part of the square of the resolved velocity gradient tensor. Here $C_w = 0.325$ is the model constant and $\Delta = (\Delta x_1 \Delta x_2 \Delta x_3)^{1/3}$ is the local mesh size. Among the variety of SGS viscosity models, the one selected automatically provides the correct $\bar{\mu}_{\text{SGS}} / \bar{\mu} \sim \mathcal{O}(y^+)^3$ asymptotic behavior in the near-wall region without prescribing any artificial transition between the bulk flow and the boundary layer.

Finally, the SGS term of the filtered energy equation is given by

$$E_j^{\text{SGS}} = \overline{(\rho E + p) u_j} - (\bar{\rho} \tilde{E} + \bar{p}) \tilde{u}_j \quad (8a)$$

$$= \underbrace{[\rho c_p T u_j - \bar{\rho} c_p \tilde{T} \tilde{u}_j]}_{\mathcal{Q}_j} + \underbrace{[\frac{1}{2} (\overline{\rho u_i u_i u_j} - \bar{\rho} \tilde{u}_i \tilde{u}_i \tilde{u}_j)]}_{\psi_{ij}} - \frac{1}{2} T_{ii}^{\text{SGS}} \tilde{u}_j. \quad (8b)$$

Here $\mathcal{Q}_j = -\lambda_{\text{SGS}} \partial \tilde{T} / \partial x_j$ is the SGS heat flux, modeled with $\lambda_{\text{SGS}} = \mu_{\text{SGS}} \gamma R / (\gamma - 1) / \text{Pr}_{\text{SGS}}$, while ψ_{ij} denotes the velocity triple correlation tensor the contribution of which has been set to zero. The SGS Prandtl number Pr_{SGS} is assumed equal to 0.9.

A. Equilibrium wall-stress model

The wall model assumes equilibrium between convection and pressure gradient and is characterized by two unknowns, U_{WM} and T_{WM} , which denote the averaged wall-parallel velocity and temperature, respectively. The subscript WM is used to emphasise that the quantity is obtained using

the wall model and not the LES solver. Under the equilibrium hypothesis [17], the Navier-Stokes equations result in the following ordinary differential equations (ODE) system:

$$\frac{d}{dy} \left[(\mu_{\text{WM}} + \mu_{t,\text{WM}}) \frac{dU_{\text{WM}}}{dy} \right] = 0, \quad (9a)$$

$$\frac{d}{dy} \left[c_p \left(\frac{\mu_{\text{WM}}}{\text{Pr}} + \frac{\mu_{t,\text{WM}}}{\text{Pr}_{t,\text{WM}}} \right) \frac{dT_{\text{WM}}}{dy} \right] = -\frac{d}{dy} \left[(\mu_{\text{WM}} + \mu_{t,\text{WM}}) U_{\text{WM}} \frac{dU_{\text{WM}}}{dy} \right] \quad (9b)$$

where c_p is the specific heat at constant pressure, $\text{Pr}_{t,\text{WM}} = 0.9$ is the model turbulent Prandtl number, $\mu_{\text{WM}} = \mu_{\text{WM}}(T_{\text{WM}})$ is the laminar viscosity which obeys Sutherland's law, and $\mu_{t,\text{WM}}$ is the model eddy viscosity, defined as

$$\mu_{t,\text{WM}} = \kappa \rho_{\text{WM}} u_\tau y^+ D, \quad (10)$$

where $\kappa = 0.41$ is the von Kármán constant and $\rho_{\text{WM}} = p_{\text{LES}}/T_{\text{WM}}$ denotes the density profile, obtained assuming a constant pressure distribution in the boundary layer. The Van Driest damping function, D , is given by

$$D = [1 - \exp(-y^+/A^+)]^2 \quad (11)$$

where $A^+ = 17$ is a model constant indicating the dimensionless height above the wall where the molecular and turbulent viscosities become of the same order of magnitude. Under the equilibrium assumption, the bracketed quantities in Eqs. (9a) and (9b) are constant across the wall-modeled layer. These conserved quantities correspond to the sum of the viscous and turbulent shear stress [Eq. (9a)] and the sum of molecular diffusivity, turbulent heat transport [left-hand side of Eq. (9b)], and aerodynamic heating [right-hand side of Eq. (9b)]. The ODE system needs to be solved on an independent grid that goes from the wall $y = 0$, where the following boundary conditions are imposed,

$$U_{\text{WM}} = 0, \quad (12a)$$

$$T_{\text{WM}} = T_w \text{ (isothermal wall) or } \frac{dT_{\text{WM}}}{dy} = 0 \text{ (adiabatic wall)}, \quad (12b)$$

to a matching location $y = h_{\text{wall}}$, where the corresponding boundary conditions are

$$U_{\text{WM}} = u_{\text{LES}}, \quad (13a)$$

$$T_{\text{WM}} = T_{\text{LES}}, \quad P_{\text{WM}} = p_{\text{LES}} \quad (13b)$$

where u_{LES} , T_{LES} , and p_{LES} are the resolved LES values of wall-parallel velocity, static temperature, and static pressure, respectively. The equilibrium model is used to compute the wall shear stress and the wall heat flux defined as

$$\tau_{w,\text{WM}} = \left(\mu \frac{dU_{\text{WM}}}{dy} \right)_{y=0}, \quad q_{w,\text{WM}} = \left(\frac{c_p \mu}{\text{Pr}} \frac{dT_{\text{WM}}}{dy} \right)_{y=0}. \quad (14)$$

The information is then fed back as a boundary condition to the outer LES grid as detailed in the next sections.

B. Unified WR and WMLES methodology

WMLES models have been developed with the explicit intention of placing the first grid point as far as possible from the wall location. This represents the strength of the WM approach, but also its weakness since any relation with the standard no-slip boundary condition for the velocity field or isothermal and adiabatic conditions for the temperature is wholly lost, and the role of the boundary is packed into the model wall shear stress, $\tau_{w,\text{WM}}$, and heat flux, $q_{w,\text{WM}}$. Neglecting the no-slip condition is strongly penalizing for those flow regions where the near-wall dynamics could

be resolved rather than being fully modeled, even employing a sufficiently coarse grid: that is the case of incipient separating or laminar portions of wall layers. In these cases, the wall shear stress is close to zero, resulting in local resolutions that often fall within wall-resolved criteria.

In the proposed method, the key for blending the WR and WM approaches relies on the modification of the overall viscosity $\mu_{\text{tot}} = \mu + \mu_{\text{SGS}}$ and diffusivity $\lambda_{\text{tot}} = \lambda + \lambda_{\text{SGS}}$ at the wall location in such a way that the allowable shear stress and heat flux are fed back to the outer LES field simultaneously keeping no-slip and no-penetration and isothermal and adiabatic boundaries active.

Looking at the filtered NS equations, μ_{SGS} and λ_{SGS} are free parameters for the system which solely depend on the choice of the turbulence model and are subject to the constraint of being *wall-turbulence consistent*, i.e., they have to vanish moving towards the wall gradually. More specifically, this condition must be respected in the case of a purely WR simulation, where the near-wall resolution is sufficient to capture the smallest turbulent structures adequately. Conversely, if the near-wall resolution does not provide a WR condition, the wall-consistency constraint must be dropped and the SGS coefficients (μ_{SGS} , λ_{SGS}) can assume a nonzero value at the wall location to provide the SGS contributions not captured by the discretization scheme. Therefore, for the development of a unified WR and WMLES strategy, it is essential to understand how to assign values to the overall wall viscosity ($\mu_w^{\text{tot}} = \mu_w + \mu_w^{\text{SGS}}$) and diffusivity ($\lambda_w^{\text{tot}} = \lambda_w + \lambda_w^{\text{SGS}}$) to meet this complex set of requirements. Let us consider the following quantities:

$$\mu_{\text{eff}} = \frac{\tau_{w,\text{WM}}}{\tau_w^{\text{LES}}} \mu_w, \quad (15a)$$

$$\lambda_{\text{eff}} = \frac{q_{w,\text{WM}}}{q_w^{\text{LES}}} \lambda_w, \quad (15b)$$

which could be called *effective wall viscosity* and *effective wall heat diffusivity*. Equation (15a) represents the laminar wall viscosity corrected by the ratio between the model ($\tau_{w,\text{WM}}$) and the resolved LES shear stress (τ_w^{LES}). Similarly, Eq. (15b) denotes the laminar wall diffusivity corrected by the ratio between the model ($q_{w,\text{WM}}$) and the LES heat fluxes (q_w^{LES}). These equations can be physically interpreted as the missing SGS contributions at the wall location which provide the desired wall shear stress and heat flux for the LES outer field according to

$$\tau_w^{\text{LES}} = \mu_{\text{eff}} \frac{\partial u_f}{\partial y} = (\mu_w + \mu_w^{\text{SGS}}) \frac{\partial u_f}{\partial y}, \quad (16a)$$

$$q_w^{\text{LES}} = \lambda_{\text{eff}} \frac{\partial T}{\partial y} = (\lambda_w + \lambda_w^{\text{SGS}}) \frac{\partial T}{\partial y}. \quad (16b)$$

Therefore, in the case of WMLES, the SGS viscosity and diffusivity at the wall location are not null and their values

$$\mu_w^{\text{SGS}} = \mu_{\text{eff}} - \mu_w, \quad (17a)$$

$$\lambda_w^{\text{SGS}} = \lambda_{\text{eff}} - \lambda_w \quad (17b)$$

precisely denote the missing SGS contribution at the wall. These quantities can be fed back to the LES outer field, correcting the velocity and temperature gradients by a factor that provides the desired shear stress and heat flux at the wall location. In contrast, in the WRLES case, the effective viscosity and diffusivity automatically recover the corresponding laminar values, guaranteeing $\mu_w^{\text{SGS}} = \lambda_w^{\text{SGS}} = 0$. This arrangement effortlessly unifies the WRLES and the WMLES approaches, keeping active both the no-slip and no-penetration conditions for the velocity field and the isothermal and adiabatic condition for the temperature at the wall. Moreover, the general character of the proposed methodology makes possible an easy coupling with most of the numerical implementations since the SGS viscosity and diffusivity fields are locally modified depending on the near-wall resolution.

III. NUMERICAL METHODS

A. Numerical treatment of the filtered Navier-Stokes equations

The filtered Navier-Stokes equations are discretized through high-order finite difference schemes on Cartesian grids. The nonlinear convective terms are based on a sixth-order, central discretization [34] which provides semidiscrete preservation of the total kinetic energy in the limit of inviscid, incompressible flows. This property allows for a robust spatial discretization of the convective derivatives without the addition of numerical dissipation. Hence, the numerical method is ideal in the context of LES, where the dissipation must be provided only by the SGS model to avoid uncertainty related to the role of the numerical discretization in the prediction of the turbulent fluctuations. The method has been successfully applied to simulate a wide range of compressible wall-bounded flows (see, e.g., [29,35–37]).

A peculiarity of the numerical discretization relies on the treatment of the viscous fluxes, expanded in a semiconservative formulation and discretized with sixth-order finite differences. Here a brief description of the method is reported, while further details can be found in De Vanna *et al.* [38]. The viscous terms can be recast as

$$\frac{\partial \bar{\tau}_{ij} - T_{ij}^{\text{SGS}}}{\partial x_j} = \underbrace{\frac{\partial}{\partial x_j} \left(\bar{\mu}_{\text{tot}} \frac{\partial \tilde{u}_i}{\partial x_j} \right)}_{\text{Incompressible contribution}} + \underbrace{\frac{\partial}{\partial x_j} \left(\bar{\mu}_{\text{tot}} \frac{\partial \tilde{u}_j}{\partial x_i} - \frac{2}{3} \bar{\mu}_{\text{tot}} \frac{\partial \tilde{u}_s}{\partial x_s} \delta_{ij} \right)}_{\text{Compressible contribution}}. \quad (18)$$

The *incompressible contribution* acts in any flow conditions, while the *compressible contribution* is expected to assume large values just near shocks. Here $\bar{\mu}_{\text{tot}} = \bar{\mu} + \mu_{\text{SGS}}$ is the overall viscosity. Usually, the viscous fluxes are discretized via a standard collocated approach, a numerical description which is well known for providing erroneous behaviors of the flow and instabilities especially in poorly resolved regions or where the $\bar{\mu}_{\text{tot}}$ experiences highly local variations. This inconvenience is highly mitigated if a conservative formulation accounts for the *incompressible contribution*; thus, we can write

$$\frac{\partial}{\partial x} \left(\bar{\mu}_{\text{tot}} \frac{\partial \tilde{u}}{\partial x} \right) \simeq \frac{1}{\Delta x_i} (\hat{\tau}_{i+1/2} - \hat{\tau}_{i-1/2}). \quad (19)$$

Here $\hat{\tau}_{i+1/2}$ denotes a high-order representation of the viscous stresses at the cell interface expressed as

$$\hat{\tau}_{i+1/2} = \frac{1}{\Delta x_{i+1/2}} \sum_{l=m}^n \beta_l \bar{\mu}_{i+1} \gamma_l \tilde{u}_{i+1} \quad (20)$$

where $\{\beta_l, \gamma_l\}_{l=m}^n$ denote the interpolation coefficients as reported by De Vanna *et al.* [38]. In the case of uniform viscosity, the method recovers a standard collocated description of the viscous terms with corresponding order of accuracy. Besides, in the limit of incompressible or weakly compressible flows, the proposed approach provides the high-order conservation of the viscous terms independently to the grid stretching and resolution or the viscosity variations. The scheme is also employed in the numerical treatment of the heat flux components observing that

$$\frac{\partial}{\partial x} \left(\bar{\lambda}_{\text{tot}} \frac{\partial \tilde{T}}{\partial x} \right) \simeq -\frac{1}{\Delta x_i} (\mathcal{J}_{i+1/2} - \mathcal{J}_{i-1/2}) \quad (21)$$

is structurally similar to the one given in Eq. (19).

Finally, the solution is advanced in time with the third-order low-storage total variation diminishing Runge-Kutta method by Gottlieb and Shu [39]. The scheme provides a maximum Courant-Friedrich-Lewy parameter CFL_{max} equal to 1. In the following computations, the CFL number is set equal to 0.5.

B. Numerical treatment of the wall-stress model

The focus of the paper is to develop an algorithm that guarantees a smooth transition between WMLES and WRLES, leaving the freedom to use a grid compatible with the available computational resources. During the simulation, a dynamical procedure checks if the near-wall resolution satisfies WRLES mesh requirements. In this respect, even though sharp thresholds between WR and non-WR cases cannot be expressed, it is necessary to select upper bounds beyond which wall resolutions (i.e., Δx_w^+ , Δy_w^+ , and Δz_w^+) are not considered adequate for a WR approach. Therefore, based on recommendations available in literature [40,41], we consider a case sufficiently resolved when

$$\Delta x_w^+ < 50, \quad \Delta y_w^+ < 5, \quad \Delta z_w^+ < 25. \quad (22)$$

The dynamic procedure computes a first guess of the local viscous length, δ_v , using Reichardt's law [42]

$$\frac{\tilde{u}_j}{u_\tau} = \kappa^{-1} \log(1 + \kappa y^+) + 7.8 \left(1 - e^{-\frac{y^+}{11}} - y^+ \frac{e^{-0.33y^+}}{11} \right) \quad (23)$$

that is solved by providing the resolved LES wall-parallel velocity (\tilde{u}_j) at a fixed wall distance y_0 , with $y^+ = y_0/\delta_v$. Even if Eq. (23) assumes equilibrium of the flow, the model generalizes the standard von Kármán log law and can be applied to out-of-equilibrium conditions as long as the y^+ input location is taken in the viscous, the buffer, or the log-law regions of the boundary layer. Once the solution of Reichardt's law is obtained, the δ_v value is employed to evaluate the near-wall resolution and discern if the local boundary layer requires a WR or a WM treatment. It is worth pointing out that when grid refinement progressively increases from the purely WM to the WR case it is likely that the matching location of the wall model h_{WM} (usually taken as a fixed location in the LES grid in a purely WMLES configuration [43]) falls inside the buffer layer. This region is not suitable to act as an exchange location with the LES field since it is characterized by extreme velocity and pressure fluctuations. To avoid this occurrence, the WM-matching location, j_{int} , is identified by the condition of being at least the third off-the-wall point and having a y_j^+ value greater than 40. Thus, the following condition holds:

$$j_{int} = \left\{ j \geq 3 \mid y_j^+ = \Delta y_w^+ \frac{y_j - y_w}{y_1 - y_w} > 40 \right\}. \quad (24)$$

From preliminary tests on high-Reynolds cases, we found that placing the interface in the range $y^+ = 40 \div 500$ lead to similar results. Moreover, Eq. (24) avoids the first two points off the wall to be selected as WM interfaces, a condition that is strongly recommended to limit or reduce the log-layer mismatch [17,43].

A sketch of possible situations concerning the location of the wall-model–LES interface is reported in Fig. 1 for the wall-normal direction. Figure 1(a) is representative of a setup in which the grid places enough nodes in the near-wall region to satisfy the WR condition. Thus, the shear stress model acts sporadically since the WM procedure and the integration of Eqs. (9) is mostly skipped by the algorithm. Figure 1(b) is representative of a mixed WR and WMLES eventuality. In this case, the near-wall resolution is not able to entirely satisfy the WR condition, and the shear stress model acts quite often. However, the WMLES exchange location is still placed sufficiently far from the first grid point, the matching location being set at $y^+ \approx 40$. Finally, the third case [Fig. 1(c)] shows a purely WMLES setup. In this condition, the number of nodes is not sufficient to fall in the WR case; therefore, the model acts in most of the instantaneous flow conditions and the matching location follows the suggestions provided by Kawai and Larsson [43].

After the local near-wall resolution has been estimated and the matching location identified, the wall-stress model is applied to obtain shear stress and heat flux at the wall. As mentioned, the ODE system in Eq. (9) is solved using an independent one-dimensional finite volume (FV) grid with the

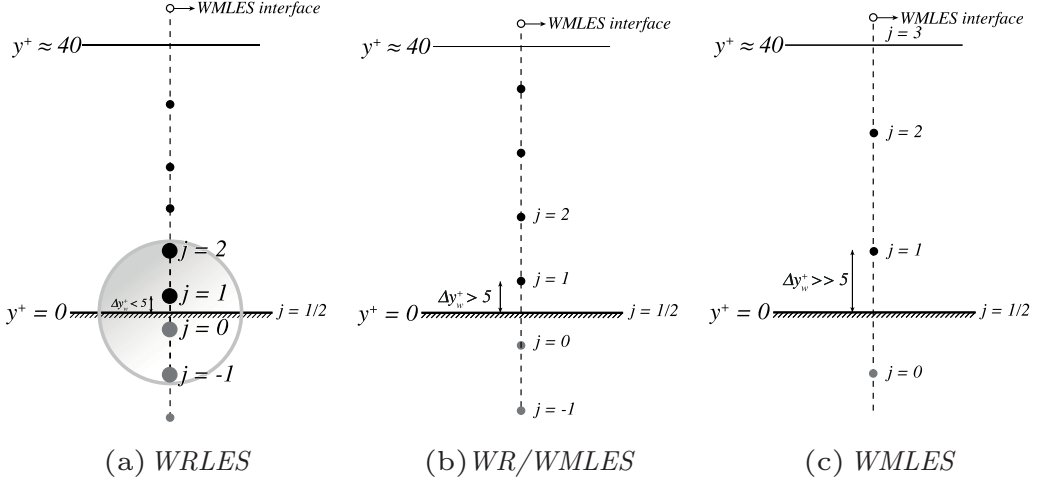


FIG. 1. Sketch of representative cases for the location of the wall-model–LES interface: (a) fully wall-resolved case, (b) mixed wall-resolved and wall-modeled case, and (c) fully wall-modeled case.

proper near-wall resolution, defined by the distribution

$$y_{f,J} = \Delta y_w \frac{r^J - 1}{r - 1}, \quad J = 0, 1, \dots, n_{\text{WM}} \quad (25)$$

where $y_{f,J}$ is the coordinate of the J th cell face, r is the stretching parameter, $\Delta y_w / \delta_v = 0.1$ is the spacing at the wall, and $n_{\text{WM}} = 50$ is the total number of nodes. The wall-model equations are solved according to the implementation described in Kawai and Larsson [43]. After obtaining $\tau_{w,\text{WM}}$ and $q_{w,\text{WM}}$, their values are fed back to the LES solver through the *effective viscosity* and the *effective heat diffusivity* defined in Eq. 15, used to locally modify the overall values at the wall ($\mu_w^{\text{tot}} = \mu_w + \mu_w^{\text{SGS}}$, $\lambda_w^{\text{tot}} = \lambda_w + \lambda_w^{\text{SGS}}$). Specifically, the practical implementation in our FD solver is based on the definition of the overall viscosity in the ghost nodes according to

$$\mu_{1-j,\text{gh}}^{\text{tot}} = 2\mu_{\text{eff}} - \mu_{j,\text{in}}^{\text{tot}} \quad j = 1, \dots, 3 \quad (26)$$

where $\mu_{j,\text{in}}^{\text{tot}}$ is the overall viscosity in correspondence to an inner point location. This method is found to be very effective in terms of stability since it does not directly alter the resolved LES fields, but it locally modifies the quantities provided by the SGS model.

IV. RESULTS AND DISCUSSIONS

In this section, the main results obtained using the proposed unified WR and WMLES approach are presented and discussed. The method is applied to channel flow configurations in both the low-speed and high-speed regime and spatially developing supersonic boundary layers.

A. Turbulent channel flow

The turbulent channel represents a fundamental benchmark for any numerical model developed to simulate wall turbulence. Here, we consider a nearly incompressible setup at $M_b = u_b / c_w = 0.1$ and a compressible one at $M_b = 1.5$ for different values of the bulk Reynolds number, i.e., $\text{Re}_b = 2\rho_b u_b h / \mu_w$. Here $u_b = 1 / (\rho_b V) \int_V \rho u dV$ is the bulk velocity, $\rho_b = 1 / V \int_V \rho dV$ is the bulk density, while μ_w and c_w are the laminar viscosity and the speed of sound at the wall location, respectively.

TABLE I. Parameters of the turbulent channel flow simulations.

Case	Re_τ	Re_b	M_b	Re_τ^*	N_x	N_y	N_z	α	Δx^+	$\Delta y_w^+ \div \Delta y_c^+$	Δz^+
0590a	590	21814	0.1	588	128	128	128	3.4	29	$0.5 \div 18$	14.5
0590b	590	21814	0.1	567	48	48	24		78	$12.3 \div 24.6$	78
0590c	590	21814	0.1	560	48	36	24		78	$16.4 \div 32.7$	78
0590d	590	21814	0.1	560	100	96	100	2.0	37.1	$3 \div 16.4$	18.5
0590e	590	21814	0.1	597	100	64	100		37.1	$9.2 \div 18.4$	18.5
0590f	590	21814	0.1	577	100	36	100		37.1	$16.4 \div 32.8$	18.5
1000a	1000	40411	0.1	910	80	36	40		78	$28 \div 56$	78
1000b	1000	40411	0.1	940	80	72	40		78	$13 \div 26$	78
1000c	1000	40411	0.1	993	160	96	120	2.6	39.2	$3 \div 32$	26.2
1000d	1000	40411	0.1	1016	160	96	60	2.6	39.2	$3 \div 32$	52.4
1000e	1000	40411	0.1	1027	160	96	30	2.6	39.2	$3 \div 32$	104.7
1000f	1000	40411	0.1	1012	120	96	160	2.6	52.3	$3 \div 32$	19.6
1000g	1000	40411	0.1	1057	60	96	160	2.6	104.7	$3 \div 32$	19.6
1000h	1000	40411	0.1	1095	30	96	160	2.6	209.4	$3 \div 32$	19.6
2000a	2000	86453	0.1	1790	160	64	80		78	$32 \div 64$	78
2000b	2000	86453	0.1	1840	160	128	80		78	$16 \div 32$	78
5200a	5200	253374	0.1	4870	160	128	80		204	$40 \div 80$	204
500a	500	14386	1.5	462	40	40	20		79	$12.5 \div 25$	79

A list with the relevant parameters of all the configurations analyzed is reported in Table I, where the bulk Reynolds number (Re_b), and the nominal and the computed friction Reynolds number (Re_τ and Re_τ^* , respectively), where $Re_\tau = \rho_w u_\tau h / \mu_w$, are also available.

The computations are carried out in a tridimensional box with size $L_x \times L_y \times L_z = 2\pi h \times 2h \times \pi h$ along the x , y , and z coordinates, respectively, h being the channel half height. A uniform mesh spacing is applied in the wall-parallel directions, whereas a nonuniform distribution is adopted in the wall-normal direction according to

$$\frac{y_j}{h} = \frac{\text{erf}[\alpha(\eta_j - \frac{1}{2})]}{\text{erf}(\frac{1}{2}\alpha)}, \quad j = 1, \dots, N_y \quad (27)$$

where $\eta_j = (j - 1/2)/N_y$ is the computational coordinate and α the stretching parameter. The number of nodes, $N_x \times N_y \times N_z$, the value of the stretching parameter, α , and the corresponding mesh spacings in inner units (i.e., normalized by the viscous length, δ_ν), $\Delta x^+ \times \Delta y_w^+ \div \Delta y_c^+ \times \Delta z^+$, are reported in Table I for all the simulations. The units in the y direction are reported as a range between the wall (Δy_w^+) and the centerline (Δy_c^+) spacings, respectively.

Concerning the boundary conditions, periodicity is enforced in the wall-parallel directions while a no-slip isothermal condition is imposed for the two walls. The grid spacing is staggered in correspondence with the first and the last cell so that the wall coincides with an intermediate node. This process guarantees mass conservation and allows one to increase the simulation time step [44]. The initial condition follows the procedure described in Dan and John [45], which superimposes a vortex pair to the analytical solution of the Poiseuille flow. This strategy promotes an early transition to turbulence. To sustain the flow rate in the channel, a forcing term $\mathcal{F} = \{0, f, 0, 0, fu\}^T$ is added to the right-hand side of the Navier-Stokes equations. The latter is evaluated at each time step. The process enforces the conservation of the mass-flow rate discretely.

1. Fully wall-resolved setup

As a first step, a nearly incompressible turbulent channel flow with a nominal friction Reynolds number equal to $Re_\tau = 590$ is simulated considering a purely WR setup. The test

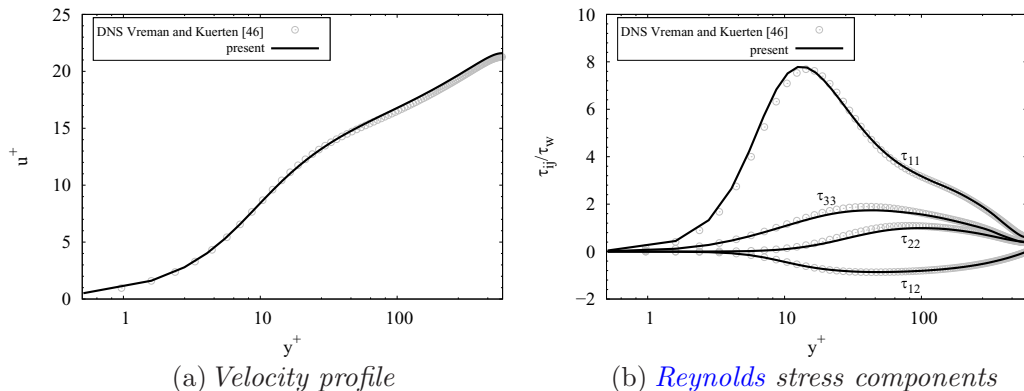


FIG. 2. WRLES of turbulent channel flow at $M_b = 0.1$ and $\text{Re}_\tau = 590$. Distribution of (a) mean velocity profiles and (b) Reynolds stresses as a function of y^+ , compared with reference DNS data by Vreman and Kuerten [46] (gray circles).

aims at validating the solver in the case of an incompressible fully resolved configuration. In this case the resolution is $\Delta x^+ = 29$, $\Delta y^+ = 0.5 \div 18$ and $\Delta z^+ = 14.5$ and the computation sees the wall model inactive since most of the energetic turbulent scales are assumed to be captured.

Figure 2 shows the mean streamwise velocity profile, $u^+ = \tilde{u}/u_\tau$, and density-scaled Reynolds stress components, $\bar{\tau}_{ij}/\tau_w = \bar{\rho} \tilde{u}_i'' \tilde{u}_j'' / \tau_w$, as a function of the inner-scaled wall distance $y^+ = y \text{Re}_\tau$. An excellent agreement with the reference DNS data of Vreman and Kuerten [46] is observed. Moreover, the computed friction Reynolds number is found equal to $\text{Re}_\tau^* = 588$ which is 0.3% less than the target value.

2. Fully wall-modeled setup

As a second step, we assess the performance of the fully wall-modeled approach, which computes the wall shear stress, τ_w , and heat flux, q_w , without a direct computation of the near-wall turbulence dynamics. This strategy avoids extremely refining the mesh in the wall region since the computational demanding portions of the flows are completely modeled rather than being solved, and the first grid point can lie in the log layer. Even if the wall resolution drastically drops, the large-scale dynamics and the energy-dominant turbulent structures are still directly resolved by the off-wall LES. The process preserves the proper energy exchange between the vortex scales and captures the turbulent time-varying dynamics.

The effectiveness of the model can be appreciated looking at Figs. 3 and 4, where the mean streamwise velocity profile and the density scaled Reynolds stress components are shown, respectively. Both figures report the data as a function of the inner-scaled wall distance for several cases in the low-Mach regime. The computations span a wide space of Reynolds numbers ($\text{Re}_\tau = \{590, 1000, 2000, 5200\}^T$), ranging from the low to the moderate to high regime. Details in terms of grid points and resolution are given in Table I, cases 590b, 590c, 1000a, 1000b, 2000a, 2000b, and 5200a. The filtered Navier-Stokes equations are discretized on uniform grids only, avoiding wall refinements and placing the first grid node sufficiently far from the wall.

Overall the results are in good agreement with the reference DNS data, showing only small discrepancies, especially for the mean velocity profile, that is affected by a mild log-layer mismatch. In particular, an upward shift is present in the WMLES data, with the model showing some difficulties in accurately reproducing the target friction Reynolds number. It is worth pointing out that the log-layer mismatch is a major issue in the field of WMLES since the problem has not been entirely ascertained yet. In this regard, various studies suggest that, within the WM paradigm, both positive

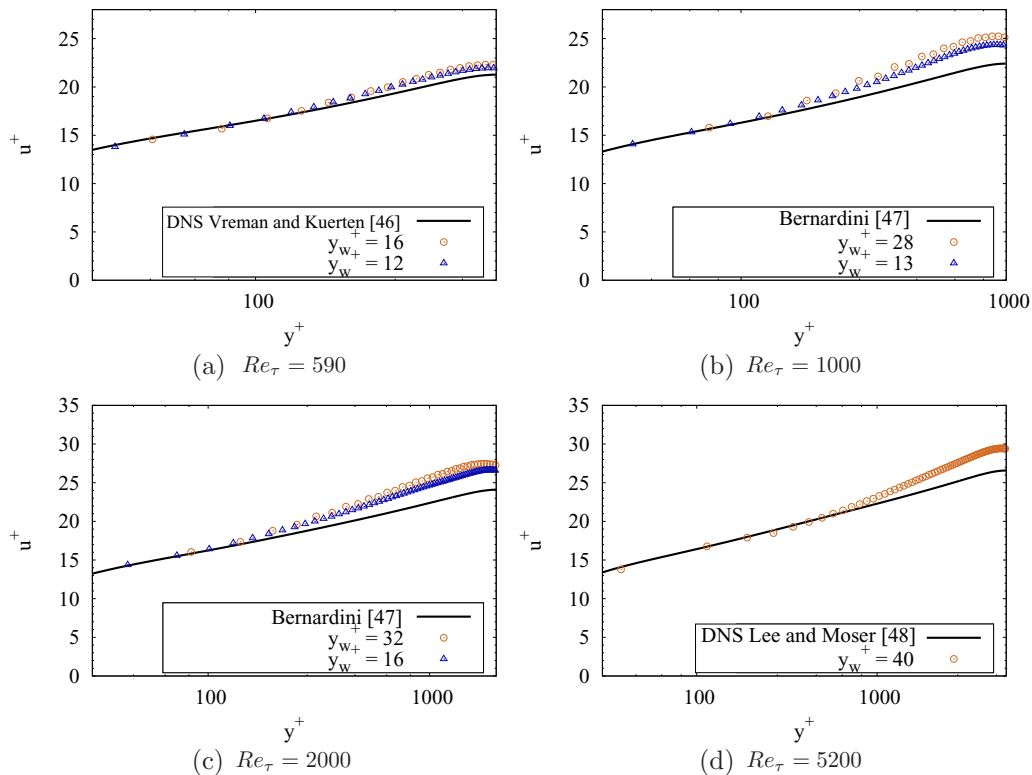


FIG. 3. Mean streamwise velocity profiles $u^+ = \bar{u}/u_\tau$ for channel flow cases at $M_b = 0.1$ and various Reynolds numbers. Present results (symbols) are compared with DNS data from Vreman and Kuerten [46], Bernardini *et al.* [47], and Lee and Moser [48] (solid lines).

and negative mismatches are possible, depending on numerous factors. First, the mesh should be accurately calibrated to minimize the phenomenon and reduce the under- and overprediction of the skin friction. This process can undoubtedly be conducted in canonical configurations but can rarely be employed in complex geometries. Secondly, different code implementations (e.g., FD vs FV), numerical methods, and turbulence models can have an influence on this issue, making it still an open problem (see, e.g., Larsson *et al.* [17] and Yang *et al.* [49] for further details). However, the coarsest setup provides a predicted shear Reynolds number (i.e., Re_τ^* in Table I) with a 10% error compared to DNS, which could be considered well within the range of acceptability in engineering applications.

Finally, as shown in Fig. 4, velocity fluctuation intensities away from the wall exhibit an excellent agreement against DNS data whereas the near-wall fluctuations in the unresolved inner layer are not computed. This implies that the wall model works as expected, creating physically realistic fluctuations of the resolved turbulence far from the wall without resolving the near-wall region. However, since the interface between the wall model and the LES field is always placed some point far from the wall location, the first few WMLES nodes do not accurately represent the actual solution and could be considered a *starting region* for the model itself.

3. Wall-resolved and wall-modeled setup

Following the purely WRLES and purely WMLES results, this section aims at illustrating the principal feature of the proposed method: the ability to smoothly switch from a WR to a WM configuration in the context of LES. For the sake of clarity, we first investigate the effect of

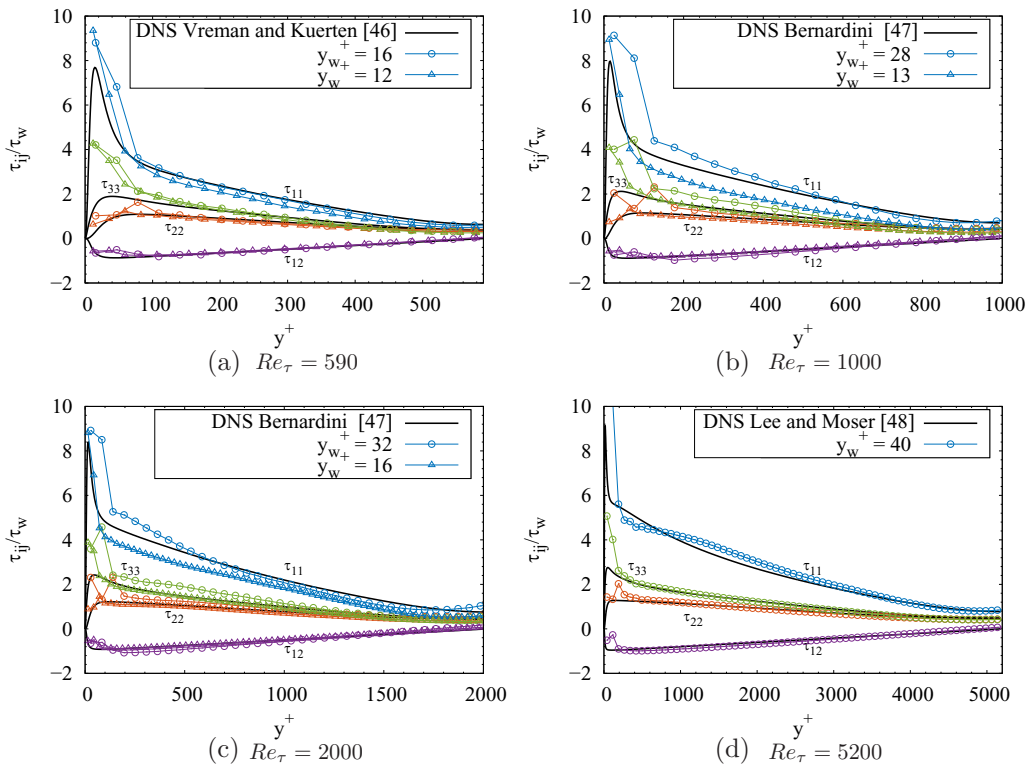


FIG. 4. Density scaled Reynolds stress components $\bar{\rho} \widetilde{u_i' u_j'} / \tau_w$ as a function of the inner scaled wall distance y^+ for channel flows at $M_b = 0.1$ and different Reynolds numbers. Present results (symbols) are compared with DNS data from Vreman and Kuerten [46], Bernardini *et al.* [47], and Lee and Moser [48] (solid lines).

the transition in the wall-normal direction, being the most critical of the three concerning wall turbulence modeling. Then, we will focus on the impact of a low resolution in the wall-parallel directions.

a. Effect of the wall-normal resolution. Several simulations of the low-speed channel at $Re_\tau = 590$ are performed using a set of grids with a decreasing wall-normal resolution. In particular, the computations are performed setting the precomputed Δy_w^+ in the range $\{3, 9.2, 16.4\}^T$ and imposing that the wall-parallel spacings do not exceed the bounds expressed by Eq. (22). The setup corresponds to a coarse WR, mixed WR and WM conditions, and a purely WM arrangement exploiting the full-range capabilities of the proposed numerical method. The details of the computations are reported in Table I, cases 0590d–0590f. The comparison of the results with the incompressible reference DNS by Vreman and Kuerten [46], reported in Fig. 5, shows a good agreement for all cases. In particular, it is highlighted that the proposed numerical method can link the WR and the WM approach smoothly, without any undesired effect even when the first grid point is placed inside the buffer layer.

Figure 6 shows the near-wall turbulent structures in terms of streamwise velocity contours (i.e., \tilde{u}/c_w) in a wall-parallel plane at two different locations, $y^+ \simeq 20$ and 100. It can be observed that, as Δy_w^+ decreases, the near-wall streaks become more detailed and qualitatively recover the shape of those captured by the WRLES. In contrast, WMLES resolutions do not adequately represent the near-wall streaks, however far from the wall, at $y^+ \simeq 100$, the structure of the velocity fluctuations appears similar to WRLES cases. To quantitatively analyze the size of the turbulent structures predicted by the unified WR and WMLES simulations, the two-point spanwise correlation of the

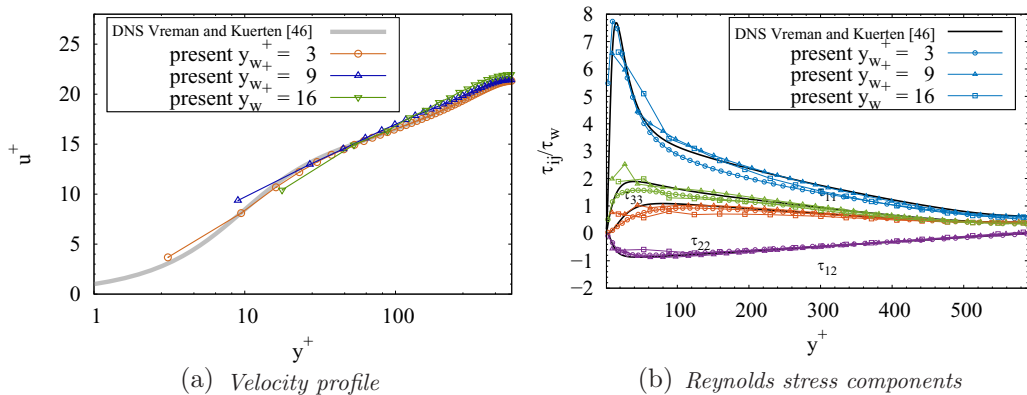


FIG. 5. Mean velocity profiles (a) and Reynolds stresses (b) from unified WR and WMLES simulations of turbulent channel flow at $M_b = 0.1$ and $Re_\tau = 590$, compared with incompressible DNS data of Vreman and Kuerten [46].

streamwise velocity fluctuations is computed as

$$R_{11}(y, \Delta z) = \frac{\overline{u_1''(x, y, z)u_1''(x, y, z + \Delta z)}}{\overline{u_1''(x, y, z)u_1''(x, y, z)}} \quad (28)$$

Contours of R_{11} are reported in Fig. 7 as a function of the spacing Δz and the wall-normal location for the various unified WR and WMLES cases compared with the pure WRLES results (solid black lines). As expected in WMLES, the structure of the turbulent field is not captured in the near-wall region, the mesh resolution being not sufficient to resolve the small spacing between the streaks. However, when moving away from the wall, all cases tend to fall back into the prediction of a standard WRLES approach. In conclusion, almost independently of the Δy_w^+ , the outer turbulent dynamics are well captured, and the model still provides the correct assessment of the boundary condition and the proper behavior of the turbulent structures.

b. Effect of the wall-parallel resolution. Since the proposed unified WR and WMLES method provides nonzero SGS contributions at the wall location according to Eq. (22), the present section aims at analyzing the behavior of the model in cases where the wall-normal grid is sufficiently fine (i.e., $\Delta y_w^+ < 5$) but the x and z directions are relatively coarse (i.e., $\Delta x^+ > 50$ or $\Delta z^+ > 25$). Near-wall turbulence is inherently three-dimensional, and such arrangements indeed would induce a considerable underestimation of the wall friction if a vanishing SGS viscosity would be prescribed.

To systematically investigate the problem, keeping the computational time affordable, a turbulent channel at a nominal friction Reynolds number equal to $Re_\tau = 1000$ is here considered. The spanwise and the streamwise resolution role is independently analyzed, keeping the other directions below the WR thresholds. The tests refer to cases 1000c–1000e (i.e., the *coarse-z* setup) and 1000f–1000h (i.e., the *coarse-x* setup) as listed Table I. As usual, equally spaced grids are employed along x and z while Eq. (27) is used to cluster the point near the walls.

Figure 8 shows the results of the systematic increase of the spanwise [Fig. 8(a)] and the streamwise spacing [Fig. 8(b)]. It can be observed that the method, activating the wall model in all cases in which the wall-parallel resolution goes beyond the thresholds expressed by Eq. (22), leads to a very good comparison with the reference DNS. In particular, coarsening the grid in the spanwise direction does not seem to affect the mean velocity profile prediction, whereas a negative log-layer mismatch is visible when the streamwise resolution becomes progressively coarser. This behavior is ascribed to the very low number of nodes in the streamwise direction, which induces an incorrect representation even of the large turbulent scales.

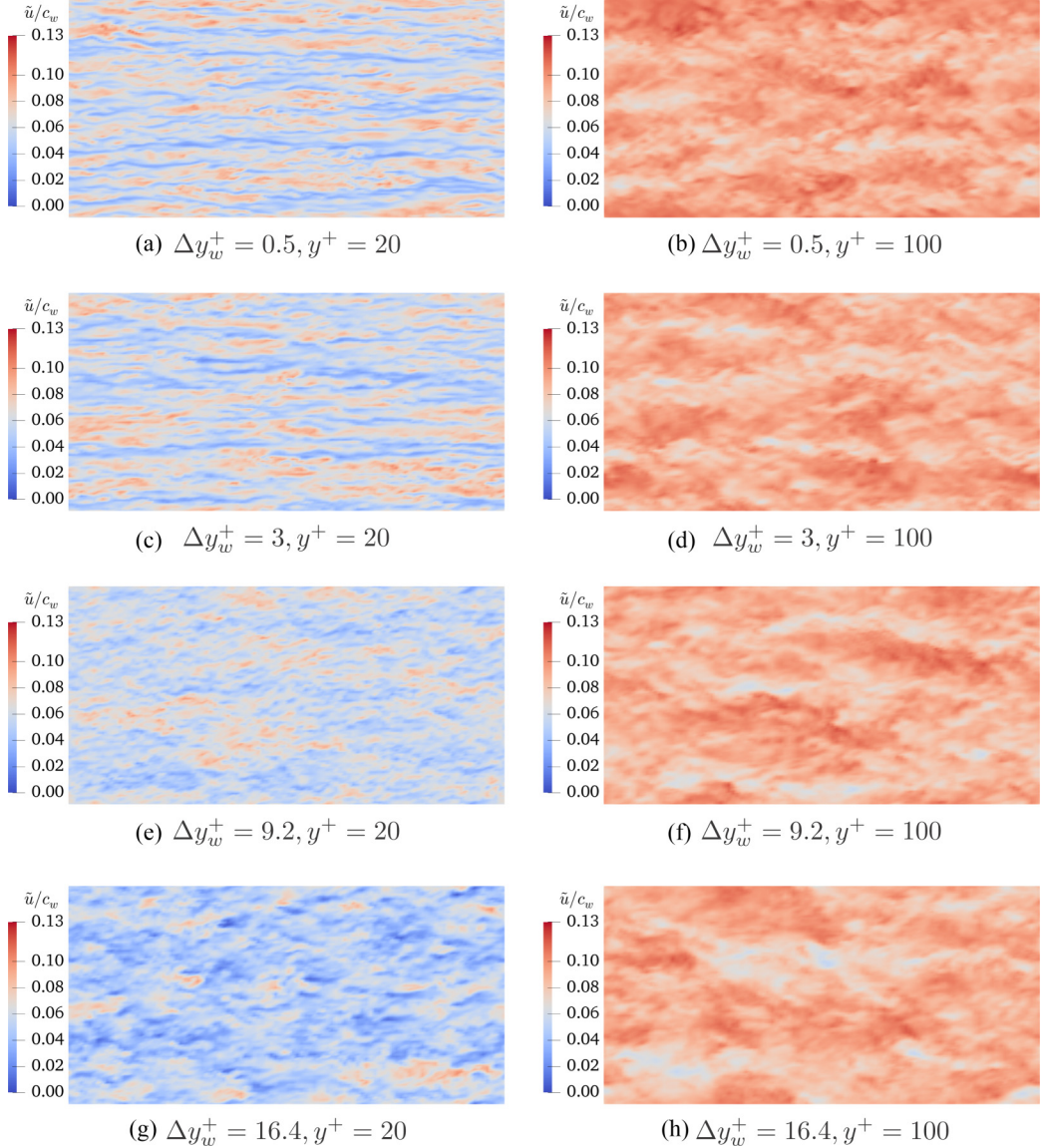


FIG. 6. Contours of instantaneous streamwise velocity in wall-parallel planes for unified WR and WMLES simulations of the turbulent channel at $\text{Re}_\tau = 590$ and $M_b = 0.1$.

c. Compressible channel flow. To conclude the tests related to the turbulent channel configuration, in this section a supersonic setup is considered. In particular, the bulk Mach number, M_b , is set equal to 1.5 while the target friction Reynolds number is $\text{Re}_\tau = 500$. To force the wall model to be switched on, the simulation is carried out on a relatively coarse grid using constant spacing in the three Cartesian directions and a number of points equal to $N_x \times N_y \times N_z$ equal to $40 \times 40 \times 20$. Such an arrangement corresponds to resolutions equal to $\Delta x^+ \times \Delta y_w^+ \times \Delta z^+ = 79 \times 12.5 \times 79$. Other details are listed in Table I, case 500a. Figure 9 reports the results of the computation in terms of mean scaled velocity profile and mean temperature as a function of the wall distance in inner scaling. In particular, blue dots show the modeled layer response average, i.e., the mean numerical solution of Eqs. (9). Red dots instead provide the resolved LES external fields. Both regions are

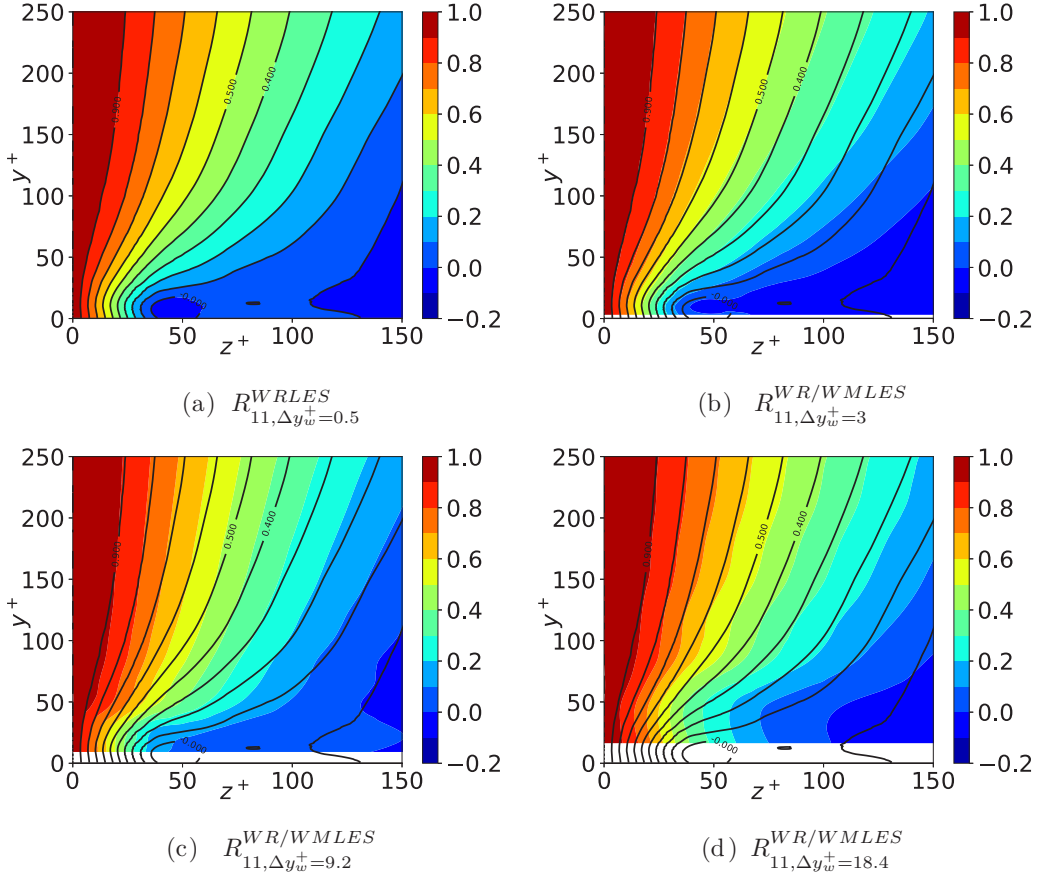


FIG. 7. Contours of the two-point spanwise correlation as a function of the spanwise shift and wall-normal location for unified WR and WMLES simulations of the turbulent channel at $Re_\tau = 590$ and $M_b = 0.1$. Solid lines denote WRLES data.

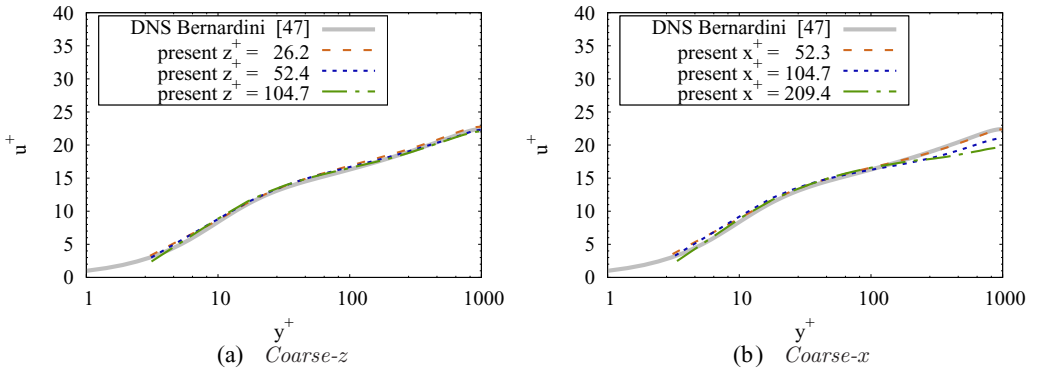


FIG. 8. Effect of the wall-parallel resolution in unified WR and WMLES simulations of turbulent channel flow. Figures 8(a) and 8(b) show mean velocity profiles as a function of y^+ with progressively coarser grid in the span- and streamwise direction, respectively. Simulation details are reported in Table I, cases 1000c–1000e and 1000f–1000h. DNS results refer to Bernardini *et al.* [47].

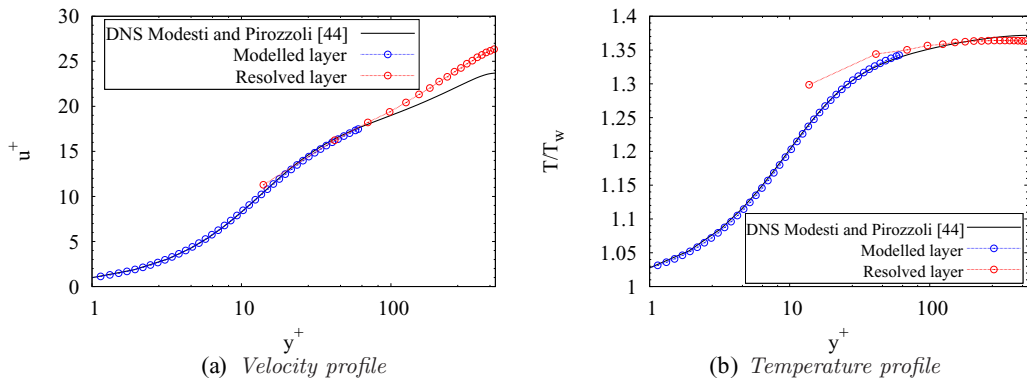


FIG. 9. Mean streamwise velocity profile (a) and mean temperature (b) as a function of y^+ for channel flow at $M_b = 1.5$ and $Re_\tau = 500$. Blue circles indicate the solution of the modeled region, red circles indicate the resolved LES region, while black solid lines denote reference DNS data by Modesti and Pirozzoli [44].

compared to DNS by Modesti and Pirozzoli [44]. A remarkable prediction of the model is obtained since both the modeled and the resolved regions exhibit a good match with the reference data. In particular, the former is in excellent agreement with DNS while the latter shows a positive mismatch in the log region, already observed for the low-speed cases.

B. Spatially developing supersonic turbulent boundary layer

As a next step, the proposed strategy is applied to predict the evolution of a spatially developing supersonic turbulent BL over a flat plate at $M_\infty = 2$ and friction Reynolds numbers up to $Re_\tau = \delta/\delta_\nu = 840$. Here δ denotes the 99% local boundary layer thickness, while $\delta_\nu = \mu_w/(\rho_w u_\tau)$ is the local viscous length. The computation is performed over a long and wide three-dimensional box of size $L_x \times L_y \times L_z = 90\delta_0 \times 10\delta_0 \times 6\delta_0$, δ_0 being the boundary layer thickness at the inflow location, where the nominal friction Reynolds number, $Re_{\tau,0}$, is also computed. The motivation for such a long domain consists of capturing the large-scale and intermittent dynamics of the boundary layer, avoiding any disturbance due to the numerical treatment of the inflow condition. An equally spaced mesh is employed in the wall-parallel directions, while a nonuniform distribution is applied in the wall-normal to cluster grid nodes towards the wall. A summary of the computational parameters is given in Table II.

The boundary conditions are specified as follows. At the top and the right boundaries of the domain, fully three-dimensional Navier-Stokes characteristic boundary conditions [50,51] are imposed. The method provides the proper outflow behavior with a minimal reflection of acoustics

TABLE II. Parameters of supersonic turbulent boundary layer simulations.

Case	Re_τ	$Re_{\tau,0}$	M_∞	N_x	N_y	N_z	Δx^+	Δy_w^+	Δz^+
250a	250	180	2	768	128	128	29.0	0.5	11.7
250b	250	180	2	256	48	32	87.9	26	46.9
250c	250	180	2	256	64	32	87.9	19	46.9
250d	250	180	2	256	96	32	87.9	13	46.9
250e	250	180	2	512	96	96	43.9	13	15.6
250f	250	180	2	512	96	96	43.9	3.0	15.6
580a	580	550	2	512	64	64	102	45	82
840a	840	550	2	512	64	64	147	65	118

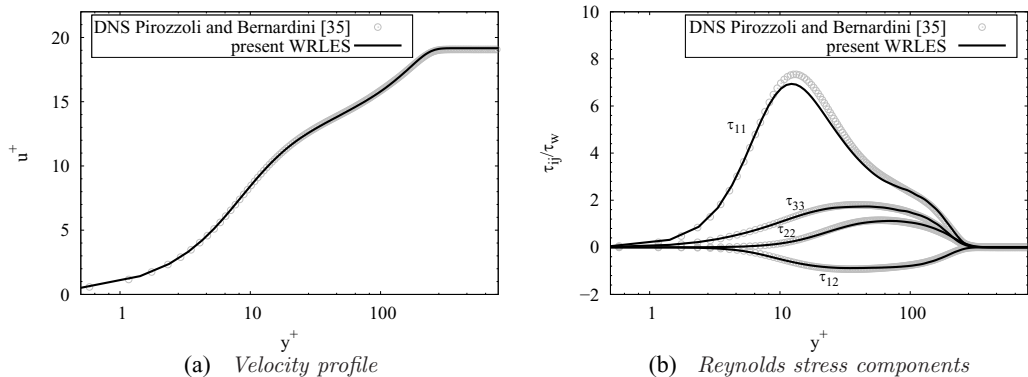


FIG. 10. WRLES of the supersonic boundary layer at $M_\infty = 2$ and $\text{Re}_\tau = 250$. Distribution of (a) mean velocity profile and (b) density-scaled Reynolds stresses as a function of y^+ , compared with reference DNS data by Vreman and Kuerten [46] (gray circles).

waves or injection of spurious disturbances. The bottom wall is also treated using a characteristic boundary condition; the velocity components are enforced to zero while the wall temperature is set equal to its nominal recovery value $T_r/T_\infty = 1 + r/2(\gamma - 1)M_\infty^2$, where $r = \text{Pr}^{1/3}$ denotes the recovery factor. Concerning the spanwise direction, the flow is assumed to be statistically homogeneous and periodic boundary conditions are applied. As far as the inflow condition, which is a crucial point in the case of spatially developing boundary layers, velocity fluctuations are superimposed to a nominal turbulent mean velocity profile. The procedure is based on the synthetic digital filter (DF) method developed by Klein *et al.* [52], that is here implemented taking into account the low-storage and optimized version of Kempf *et al.* [53]. Finally, the computation is initialized by prescribing a fully developed turbulent boundary layer using the Van Driest transformation on a velocity profile of the Musker family [54] and perturbing the initial system with the DF approach.

1. Fully wall-resolved setup

Similarly to the channel flow analysis, a fully WR setup is first presented. In this case, a spatially developing supersonic boundary layer at $\text{Re}_{\tau,0} = 180$ is considered. Flow statistics are collected in correspondence of the location where $\text{Re}_\tau = 250$. The computation sees the wall model inactive since most of the turbulent scales are assumed to be resolved by the grid employed, characterized by $\Delta y_w^+ \simeq 0.5$. The wall-parallel spacings and the number of grid nodes are listed in Table II, case 250a.

Figures 10(a) and 10(b) show the mean streamwise velocity profile in inner units, $u^+ = \bar{u}/u_\tau$, and the density scaled Reynolds stress components, $\bar{\tau}_{ij}/\tau_w = \bar{\rho} \overline{u'_i u'_j}/\tau_w$, respectively, as a function of the wall distance $y^+ = y/\delta_v$. The WRLES data exhibit a remarkable agreement with the corresponding DNS by Pirozzoli and Bernardini [35] and only small deviations are observed for the streamwise component of the Reynolds stress in the buffer layer, the peak of which is slightly underestimated by the present WRLES.

2. Fully wall-modeled setup

In this section, we test the performance of the fully WM implementation that provides both the wall shear stress, τ_w , and the wall heat flux, q_w . In this case the inflow Reynolds number is increased up to $\text{Re}_{\tau,0} = 550$ and flow statistics are evaluated at $\text{Re}_\tau = 580$ and 840. The corresponding computational parameters are listed in Table II.

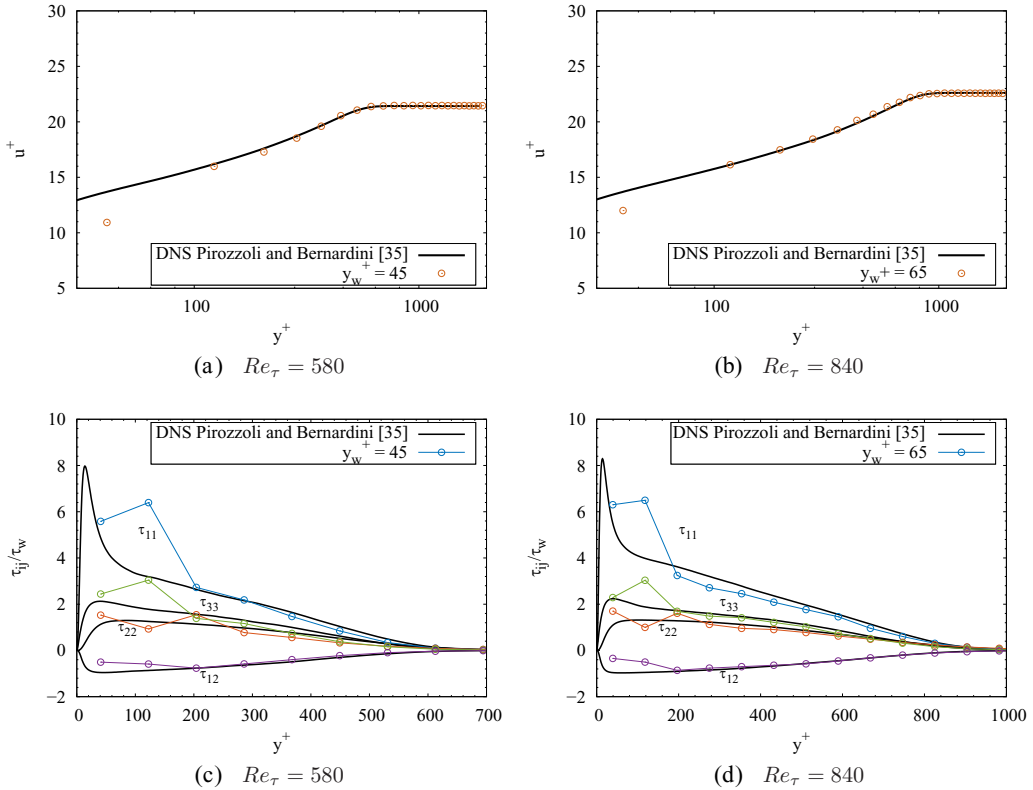


FIG. 11. Mean streamwise velocity profiles (top) and density scaled Reynolds stress components (bottom) from WMLES of the spatially developing turbulent boundary layer at $M_\infty = 2$ and various friction Reynolds numbers. Present results are compared with DNS data by Pirozzoli and Bernardini [35].

In Fig. 11, the mean streamwise velocity profile in inner units, $u^+ = \tilde{u}/u_\tau$, and the density scaled Reynolds stress components, $\bar{\rho} \overline{u'_i u'_j} / \tau_w$, are reported as a function of $y^+ = y/\delta_v$ for both friction Reynolds numbers. Present data are compared with the DNS results of Pirozzoli and Bernardini [35] at the same Mach and Reynolds conditions.

Overall the results are in excellent agreement with the DNS data in the outer layer since the WMLES model accurately predicts both the mean velocity profile and the velocity fluctuations. As observed in channel flow simulations, the first mean velocity point and the first two locations for the stress components do not show the expected behavior. As already observed for channel flows, these nodes lie below the LES-wall-stress model interface and represent a sort of *starting zone* for the computational method.

Next, we consider the spatial distribution of the skin friction coefficient. Given the lack of measurements in compressible conditions, numerical simulations of supersonic boundary layers usually compare skin friction coefficients at different Mach numbers exploiting the Van Driest II transformation [55], which allows reducing the friction coefficient, C_f , and the momentum Reynolds number, Re_θ , to incompressible values $C_{f,i}$ and $Re_{\theta,i}$ (see Hopkins and Inouke [56]). The transformed skin friction coefficient from the present WMLES is compared in Fig. 12 with a widely used empirical correlation, the Kármán-Schoenherr expression

$$C_{f,i}^{-1} = 17.08(\log_{10} Re_{\theta,i})^2 + 25.11 \log_{10} Re_{\theta,i} + 6.012. \quad (29)$$

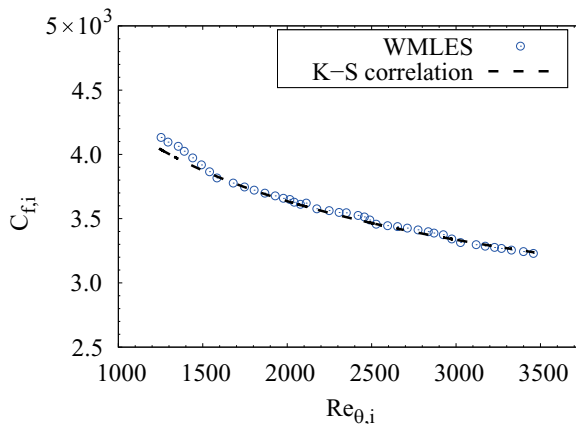


FIG. 12. Distribution of the skin friction coefficient as function of the incompressible momentum thickness Reynolds number from WMLES of the supersonic boundary layer at $M_\infty = 2$, compared with the Kármán-Schoenherr (K-S) empirical correlation.

An excellent collapse of the numerical solution to the empirical correlation can be observed, with the present data correctly reproducing the skin friction trend with the Reynolds number, thus providing further confirmation of the accuracy of the current approach.

3. Wall-resolved and wall-modeled setup

Finally, we demonstrate the capability of the present method in a mixed WM and WR setup. This feature is here assessed through low-Reynolds spatially developing BL computations in supersonic conditions with $Re_{\tau,0} = 180$ and using a decreasing resolution. In particular, the precomputed Δy_w^+ location is set in the range $\Delta y_w^+ = \{3, 13, 13(b), 19, 26\}^T$. This choice corresponds to a coarse WR, two intermediate WR and WM cases, and two purely WM configurations since the first grid point is located in the viscous, buffer, and log regions of the boundary layer, respectively. The most resolved setup adopts a nonuniform grid stretching in the wall-normal coordinate, whereas a uniform spacing is used in all the three Cartesian directions for the non-wall-resolved configurations. The statistics are collected in correspondence to the location where the friction Reynolds number assumes a value $Re_\tau = 250$. The parameters of the computations are detailed in Table II, cases 250b–250e.

The results obtained are collectively reported in Figs. 13(a) and 13(b) and compared with reference DNS data. It can be observed that the prediction of the mean streamwise velocity profile is accurate for all cases, independently of the wall resolution, and the correct near-wall behavior is recovered. Similar considerations also apply for the Reynolds stress components distribution, which is in excellent agreement with the reference except for the first two grid nodes. Therefore, it can be concluded that the present unified WR and WMLES model can successfully be applied also to the case of compressible turbulent wall-bounded flows.

V. CONCLUSIONS

A general strategy to unify the wall-resolved and wall-modeled approaches for LES of turbulent wall-bounded flows is proposed. The method ensures the no-slip and no-penetration conditions to velocity components at the wall location and allows one to impose the proper wall stress and heat transfer using *ad hoc* turbulent transport coefficients at the wall. The results show that the proposed numerical strategy falls back to the standard WR approach if the close-to-wall grid resolution is in the range of a fully resolved simulation. Conversely, the correct wall stress τ_w and heat

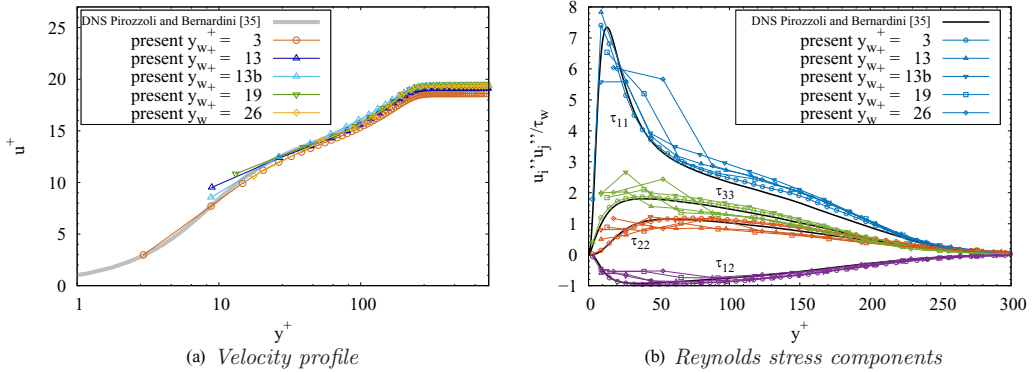


FIG. 13. Unified WR and WMLES computations of the supersonic turbulent boundary layer at $M_\infty = 2$ and $Re_\tau = 250$. Mean streamwise velocity profile (a) and density scaled Reynolds stress components (b) as a function of y^+ . Simulation details are reported in Table II, cases 250b–250f. DNS results refer to Pirozzoli and Bernardini [35].

flux q_w are provided by the WM if the near-wall region is poorly described. Thus, the method relies on a minimally intrusive process able to merge the WRLES and the WMLES approaches smoothly.

The importance of the proposed numerical strategy consists in its powerful impact for applications since it allows one to exploit the user's available computational resources, also reducing the effort in the simulation preprocessing from taking care of the treatment of the near-wall regions. In other words, given the available computational resources, the method automatically uses the more accurate WR methodology in the domain parts where the resolution is adequate while switching to WM in other regions.

The coupling methodology has been presented in the context of a finite difference flow solver based on energy preserving schemes, which guarantee virtually zero numerical dissipation in the approximation of the convective terms. This allows optimal control of the numerical discretization error, which could be critical to evaluate the accuracy of LES methods. Nonetheless, its extension to different algorithms is straightforward.

Several numerical tests have been performed by simulating two canonical wall-bounded flows, i.e., the turbulent plane channel and the spatially evolving turbulent boundary layer. In particular, the performance of the proposed methodology is intensively tested across a wide range of both Mach and Reynolds numbers and for various grid resolutions. Compared to DNS reference data, the results highlight a good accuracy in terms of both single- and two-point statistics, including mean velocity profiles, fluctuation intensities, and two-point spatial correlations in the spanwise direction. It is also shown that unified WR and WMLES simulations well reproduce the dynamics of turbulence in the outer layer, almost independently of the near-wall resolution.

Future developments will be directed to extend the proposed strategy by coupling the mixed WR and WMLES procedure with the sharp-interface immersed boundary method (e.g., De Vanna *et al.* [29]), thus allowing one to perform high-fidelity LES simulations of flows in complex geometries by using high-order finite difference methods.

ACKNOWLEDGMENTS

The authors acknowledge the IS CRA Research Infrastructure MARCONI100 based at CINECA, Casalecchio di Reno, Italy, Projects No. HP10CMQY2C IscrC URANOS3D_0 and No. HP10CM2014 INBUZZ_0, for providing the computational resources.

- [1] W. Gao, W. Zhang, W. Cheng, and R. Samtaney, Wall-modelled large-eddy simulation of turbulent flow past airfoils, *J. Fluid Mech.* **873**, 174 (2019).
- [2] F. Avanzi, F. De Vanna, Y. Ruan, and E. Benini, Design-assisted of pitching aerofoils through enhanced identification of coherent flow structures, *Designs* **5**, 11 (2021).
- [3] J. Movva, D. Papadogiannis, and S. Hiernaux, Assessment of wall modelling for large eddy simulations of turbomachinery, in *Proceedings of the ASME Turbo Expo 2018: Turbomachinery Technical Conference and Exposition*, Turbo Expo: Power for Land, Sea, and Air Vol. 2C (American Society of Mechanical Engineers, New York, 2018), doi:[10.1115/GT2018-75773](https://doi.org/10.1115/GT2018-75773).
- [4] E. Arad, N. Yokey, H. E. Brod, and D. Michaels, From supersonic combustion to thermal choking: Numerical and experimental analysis of a scramjet engine, in *Proceedings of the AIAA Aviation 2020 Forum* (AIAA, Reston, VA, 2020), p. 2966, doi:[10.2514/6.2020-2966](https://doi.org/10.2514/6.2020-2966).
- [5] M. Liefvendahl and M. Johansson, Wall-modeled LES for ship hydrodynamics in model scale, *J. Ship Res.* **65**, 41 (2020).
- [6] D. R. Chapman, Computational aerodynamics development and outlook, *AIAA J.* **17**, 1293 (1979).
- [7] H. Choi and P. Moin, Grid-point requirements for large eddy simulation: Chapman’s estimates revisited, *Phys. Fluids* **24**, 011702 (2012).
- [8] T. von Kármán, Mechanische änllichkeit und turbulenz, nachrichten von der gesellschaft der wissenschaften zu Göttingen, Math.-Physik. Klasse **1930**, 58 (1930).
- [9] G. Barenblatt, Scaling laws for fully developed turbulent shear flows. Part 1. Basic hypotheses and analysis, *J. Fluid Mech.* **248**, 513 (1993).
- [10] N. Afzal and K. Gersten, Wake layer in a turbulent boundary layer with pressure gradient: a new approach, *Fluid Mech. Appl.* **37**, 95 (1996).
- [11] P. Luchini, Universality of the Turbulent Velocity Profile, *Phys. Rev. Lett.* **118**, 224501 (2017).
- [12] B. E. Launder and D. B. Spalding, *Mathematical Models of Turbulence* (Academic Press, New York, 1972).
- [13] T. Craft, A. Gerasimov, H. Iacovides, and B. Launder, Progress in the generalization of wall-function treatments, *Int. J. Heat Fluid Flow* **23**, 148 (2002).
- [14] G. Kalitzin, G. Medic, G. Iaccarino, and P. Durbin, Near-wall behavior of RANS turbulence models and implications for wall functions, *J. Comput. Phys.* **204**, 265 (2005).
- [15] T. Knopp, T. Alrutz, and D. Schwamborn, A grid and flow adaptive wall-function method for RANS turbulence modelling, *J. Comput. Phys.* **220**, 19 (2006).
- [16] U. Piomelli and E. Balaras, Wall-layer models for large-eddy simulations, *Annu. Rev. Fluid Mech.* **34**, 349 (2002).
- [17] J. Larsson, S. Kawai, J. Bodart, and I. Bermejo-Moreno, Large eddy simulation with modeled wall-stress: Recent progress and future directions, *Mech. Eng. Rev.* **3**, 15-00418 (2016).
- [18] F. Menter, Stress-blended eddy simulation (SBES): Aa new paradigm in hybrid RANS-LES modeling, in *Symposium on Hybrid RANS-LES Methods* (Springer, New York, 2016), pp. 27–37.
- [19] W. Cabot and P. Moin, Approximate wall boundary conditions in the large-eddy simulation of high Reynolds number flow, *Flow, Turbulence and Combustion* **63**, 269 (2000).
- [20] M. Wang and P. Moin, Dynamic wall modeling for large-eddy simulation of complex turbulent flows, *Phys. Fluids* **14**, 2043 (2002).
- [21] L. Temmerman, M. A. Leschziner, C. P. Mellen, and J. Fröhlich, Investigation of wall-function approximations and subgrid-scale models in large eddy simulation of separated flow in a channel with streamwise periodic constrictions, *Int. J. Heat Fluid Flow* **24**, 157 (2003).
- [22] S. Kawai and K. Asada, Wall-modeled large-eddy simulation of high Reynolds number flow around an airfoil near stall condition, *Computers & Fluids* **85**, 105 (2013).
- [23] S. T. Bose and P. Moin, A dynamic slip boundary condition for wall-modeled large-eddy simulation, *Phys. Fluids* **26**, 015104 (2014).
- [24] G. I. Park and P. Moin, An improved dynamic non-equilibrium wall-model for large eddy simulation, *Phys. Fluids* **26**, 015108 (2014).
- [25] S. T. Bose and G. I. Park, Wall-modeled large-eddy simulation for complex turbulent flows, *Annu. Rev. Fluid Mech.* **50**, 535 (2018).

- [26] X. I. Yang and Y. Lv, A semi-locally scaled eddy viscosity formulation for LES wall models and flows at high speeds, *Theor. Comput. Fluid Dyn.* **32**, 617 (2018).
- [27] S. Krajnović and L. Davidson, Large-eddy simulation of the flow around a ground vehicle body, SAE Technical Paper No. 2001-01-0702, SAE International in United States, 2001, doi:[10.4271/2001-01-0702](https://doi.org/10.4271/2001-01-0702).
- [28] T. Mukha, S. Rezaeiravesh, and M. Liefvendahl, A library for wall-modelled large-eddy simulation based on openfoam technology, *Comput. Phys. Commun.* **239**, 204 (2019).
- [29] F. De Vanna, F. Picano, and E. Benini, A sharp-interface immersed boundary method for moving objects in compressible viscous flows, *Computers & Fluids* **201**, 104415 (2020).
- [30] F. De Vanna, F. Picano, and E. Benini, An immersed boundary method for moving objects in compressible flows, in *Direct and Large Eddy Simulation XII. DLES 2019*, edited by M. García-Villalba, H. Kuerten, and M. Salvetti, ERCOFTAC Vol. 27 (Springer, New York, 2020), pp. 291–296, doi:[10.2514/6.2021-0858](https://doi.org/10.2514/6.2021-0858).
- [31] F. De Vanna, F. Picano, and E. Benini, Large-eddy-simulations of the unsteady behaviour of a mach 5 hypersonic intake, in *Proceedings of the AIAA Scitech 2021 Forum* (AIAA, Reston, VA, 2021), p. 0858.
- [32] E. Garnier, N. Adams, and P. Sagaut, *Large Eddy Simulation for Compressible Flows* (Springer, New York, 2009).
- [33] F. Nicoud and F. Ducros, Subgrid-scale stress modelling based on the square of the velocity gradient tensor, *Flow, Turbulence and Combustion* **62**, 183 (1999).
- [34] S. Pirozzoli, Generalized conservative approximations of split convective derivative operators, *J. Comput. Phys.* **229**, 7180 (2010).
- [35] S. Pirozzoli and M. Bernardini, Turbulence in supersonic boundary layers at moderate Reynolds number, *J. Fluid Mech.* **688**, 120 (2011).
- [36] F. Salvatore, M. Bernardini, and M. Botti, GPU accelerated flow solver for direct numerical simulation of turbulent flows, *J. Comput. Phys.* **235**, 129 (2013).
- [37] D. Modesti and S. Pirozzoli, Direct numerical simulation of supersonic pipe flow at moderate Reynolds number, *Int. J. Heat and Fluid Flow* **76**, 100 (2019).
- [38] F. De Vanna, A. Benato, F. Picano, and E. Benini, High-order conservative formulation of viscous terms for variable viscosity flows, *Acta Mech.*, 1 (2021), doi:[10.1007/s00707-021-02937-2](https://doi.org/10.1007/s00707-021-02937-2).
- [39] S. Gottlieb and C.-W. Shu, Total variation diminishing Runge-Kutta schemes, *Math. Comput. Am. Math. Soc.* **67**, 73 (1998).
- [40] U. Piomelli, Wall-layer models for large-eddy simulations, *Prog. Aerospace Sci.* **44**, 437 (2008).
- [41] N. J. Georgiadis, D. P. Rizzetta, and C. Fureby, Large-eddy simulation: Current capabilities, recommended practices, and future research, *AIAA J.* **48**, 1772 (2010).
- [42] H. Reichardt, Vollständige darstellung der turbulenten geschwindigkeitsverteilung in glatten leitungen, *Zeitschrift für Angewandte Mathematik und Mechanik* **31**, 208 (1951).
- [43] S. Kawai and J. Larsson, Wall-modeling in large eddy simulation: Length scales, grid resolution, and accuracy, *Phys. Fluids* **24**, 015105 (2012).
- [44] D. Modesti and S. Pirozzoli, Reynolds and Mach number effects in compressible turbulent channel flow, *Int. J. Heat Fluid Flow* **59**, 33 (2016).
- [45] B. Dan and S. H. A. N. D. John, On turbulent spots in plane Poiseuille flow 228, 183 (1991).
- [46] A. W. Vreman and J. G. Kuerten, Statistics of spatial derivatives of velocity and pressure in turbulent channel flow, *Phys. Fluids* **26**, 085103 (2014).
- [47] M. Bernardini, S. Pirozzoli, and P. Orlandi, Velocity statistics in turbulent channel flow up to $Re_\tau = 4000$, *J. Fluid Mech.* **742**, 171 (2014).
- [48] M. Lee and R. D. Moser, Direct numerical simulation of turbulent channel flow up to, *J. Fluid Mech.* **774**, 395 (2015).
- [49] X. I. A. Yang, G. I. Park, and P. Moin, Log-layer mismatch and modeling of the fluctuating wall stress in wall-modeled large-eddy simulations, *Phys. Rev. Fluids* **2**, 104601 (2017).
- [50] T. Poinsot, Boundary conditions for direct simulations of compressible viscous flows, *J. Comput. Phys.* **99**, 352 (2004).
- [51] G. Lodato, P. Domingo, and L. Vervisch, Three-dimensional boundary conditions for direct and large-eddy simulation of compressible viscous flows, *J. Comput. Phys.* **227**, 5105 (2008).

- [52] M. Klein, A. Sadiki, and J. Janicka, A digital filter based generation of inflow data for spatially developing direct numerical or large eddy simulations, *J. Comput. Phys.* **186**, 652 (2003).
- [53] A. M. Kempf, S. Wysocki, and M. Pettit, An efficient, parallel low-storage implementation of Klein's turbulence generator for LES and DNS, *Comput. Fluids* **60**, 58 (2012).
- [54] A. J. Musker, Explicit expression for the smooth wall velocity distribution in a turbulent boundary layer, *AIAA J.* **17**, 655 (1979).
- [55] E. R. Van Driest, On turbulent flow near a wall, *J. Aeronautical Sciences* **23**, 1007 (1956).
- [56] E. J. Hopkins and M. Inouke, An evaluation of theories for predicting turbulent skin friction and heat transfer on flat plates at supersonic and hypersonic Mach numbers, *AIAA Journal* **9**, 993 (1971).